

N/O abundance ratios in gamma-ray burst and supernova host galaxies at $z < 4$. Comparison with AGN, starburst and HII regions

M. Contini

School of Physics and Astronomy, Tel Aviv University, Tel Aviv 69978, Israel

3 August 2021

ABSTRACT

The distribution of the N/O element abundance ratios calculated by the detailed modelling of different galaxy spectra at $z < 4$ is investigated. Supernova (SN) and long gamma-ray-burst (LGRB) host galaxies cover different redshift domains. N/O ratios in SN hosts increase due to secondary N production towards low z (0.01) accompanying the growing trend of active galaxies (AGN, LINER). N/O ratios in LGRB hosts decrease rapidly between $z > 1$ and $z \sim 0.1$ following the N/H trend and reach the characteristic N/O ratios calculated for the HII regions in local and nearby galaxies. The few short period GRB (SGRB) hosts included in the galaxy sample show $N/H \leq 0.04$ solar and O/H solar. They seem to continue the low bound N/H trend of SN hosts at $z < 0.3$. The distribution of N/O as function of metallicity for SN and LGRB hosts is compared with star chemical evolution models. The results show that several LGRB hosts can be explained by star multi-bursting models when $12 + \log(O/H) < 8.5$, while some objects follow the trend of continuous star formation models. N/O in SN hosts at $\log(O/H) + 12 < 8.5$ are not well explained by stellar chemical evolution models calculated for starburst galaxies. At $12 + \log(O/H) > 8.5$ many different objects are nested close to O/H solar with N/O ranging between the maximum corresponding to starburst galaxies and AGN and the minimum corresponding to HII regions and SGRB.

Key words: radiation mechanisms: general — shock waves — ISM: abundances — galaxies: GRB — galaxies: high redshift

1 INTRODUCTION

Metallicity is one of the main factors which affects the evolution of massive stars as well as their explosive death (Vergani et al 2011, Piranomonte et al 2015, Sollerman et al 2005, Woosley 1993, etc). In previous papers (e.g. Contini 2017, 2016a and references therein) we have studied the characteristic physical parameters and the element abundances of SN and GRB host galaxies at intermediate-high redshifts, $z < 4$. The sample of galaxies that was assembled in order to study the role of the main physical and chemical parameters dominating in each object (see e.g. Contini 2014 and references therein), accounts for many types, AGN, LINERs, in particular mergers, starbursts (SB), SN, GRB hosts, etc. Lyman α and UV line emitting galaxies (Contini 2015) were included to expand to the UV domain the line wavelengths from different elements and ionization levels observable throughout the redshift ranges. We have distinguished the host galaxies of SN (Contini 2016a) in different types (Ic, Ib, Ibc, IcBL, Iib, etc., Sanders et al. 2012; SLSNR, SLSNI, SLSN,

Leloudas et al, 2015) and GRB hosts (Contini 2016a, 2017) in long and short period on the basis of data by de Ugarte Postigo et al (2014), Krühler et al. (2015), Savaglio et al (2009), Han et al (2010), etc. In objects such as AGN and SB, the characteristics of the radiation flux photoionizing and heating the gas are of primary importance to understand the distribution of the gas physical conditions throughout the host galaxy. However, the element abundances are not less significant, because metallicities are related to the star formation history. SN and GRB host galaxies are also contaminated by the explosion products. The mutual influence of SN, GRB and their hosts have been discussed by Contini (2016a) who suggested that GRB hosts are less affected than the SN ones.

Metallicities in galaxies are revealed by the spectra. In previous works we compared N/H and O/H calculated for SN and GRB with those of SB, AGN and LINER galaxies as function of the redshift. We performed our investigations interpreting line and continuum spectra which con-

tained enough data to constrain the models. There are a few observed spectra at $z > 4$ that have been modelled in detail. Therefore, in this paper we investigate the evolution of N/O abundance ratios with z in different SN and GRB host galaxies focusing on relatively low redshift domain. N/O ratios are directly linked to metallicity variations and to the formation of stars. The mass of stars in a galaxy is related to its metallicity evolution (Tremonti et al. 2004). We try to explain the behaviour of N/O as function of z by the theories of Pérez-Montero et al (20013), Henry et al. (2000), Mouhcine & Contini (2002, hereafter MC02), etc. Oxygen is produced only by massive stars. Analyzing the behaviour of N/O abundance ratios as a function of metallicity in terms of O/H for Galactic and extragalactic H II region samples, Henry et al (2000) found that massive stars ($M > 8 M_{\odot}$) dominate the production of carbon, while intermediate-mass stars between 4 and $8 M_{\odot}$ dominate nitrogen production. They claim that N production is primary at low metallicities, but when $12 + \log(\text{O}/\text{H})$ exceeds 8.3, secondary N production occurs, increasing at a faster rate than O, steeper than expected for a secondary element. Moreover, they suggest that the distribution of N/O data is caused by intermittent increases in nitrogen caused by local contamination by Wolf-Rayet stars or luminous blue variables. In addition, the effect of inflow of gas into galactic systems on secondary production of nitrogen from carbon may introduce some scatter into N/O ratios at high metallicities. The evolution of N/O depends on internal star processes such as nucleosynthesis etc. Massive stars ($\sim 8\text{-}20 M_{\odot}$) are generally responsible for SN explosions and GRB in galaxies. Pérez-Montero et al claim that N/O is probably a chemical evolution indicator of single starbursts (Edmunds & Pagel 1978, Pilyugin et al 2003). The relation of N (which is a secondary element) with O (which is a primary element) is relatively independent of the chemodynamical effects such as outflows and inflows of gas from regions where star formation and element synthesis is occurring. They can be only used to explain structures of modified metallicity throughout the galaxy (Edmunds 1990). The chemical evolution of galaxies that undergo an episode of massive and rapid accretion of metal poor gas (Köppen & Hensler 2005) provides a large scatter in the N/O versus O/H diagram. Pérez-Montero & Contini (2009) found an increase of N/O with stellar mass when most of the galaxies lie in the metallicity range for the production of the secondary N. Element abundances in SN and GRB hosts as well as in the other galaxies are the product of intermingled physical events such as SN feedback, gas inflow and outflow, mergers and interactions (Pérez-Montero et al 2013). Summarizing, nitrogen is produced as a primary element in massive stars (core collapse) supernovae, then as a secondary element in WN stars and later in AGB stars. Therefore it is important to obtain the N/O results from the detailed analysis of the line spectra, in particular of the N and O characteristic lines.

The lines are emitted from gas in the physical and chemical conditions which are determined throughout the galaxy by radiation sources and dynamical effects. Notice that the emitting gas is not at a constant temperature and density, but behind the ionization fronts created by photoionization and downstream of shock fronts when collisional ionization and heating dominate, the gas recombines following the cooling rate by free-free, free-bound and line emission. All the

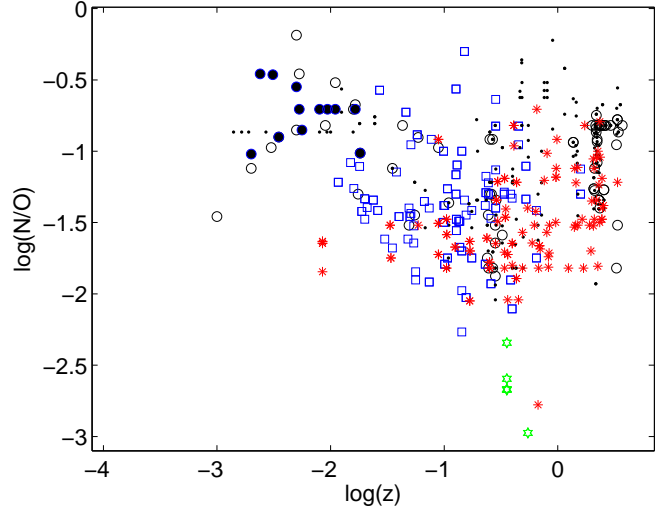


Figure 1. Distribution of N/O as function of the redshift for SN host galaxies (squares), long GRB hosts (asterisks), short GRB hosts (stars) and SB (dots), AGN (open circles) and LINERs (filled circles) both local and at higher z .

ions of different elements in different ionization levels participate to the cooling process. O^+ and O^{++} ions peak at different temperatures. Therefore, the electron temperature obtained from the $[\text{OIII}]\lambda 5007 + 4959 / [\text{OIII}]\lambda 4363$ line ratios (Osterbrock 1974) is a valid approximation for the calculation of O/H from the $[\text{OIII}]/\text{H}\beta$ line ratios, less precisely for $[\text{OII}]/\text{H}\beta$. O^+ and N^+ are linked by charge exchange reaction with H^+ because they correspond to a similar first ionization potential. Therefore O^+/O and N^+/N fractional abundances peak at the same temperatures.

The N/O results calculated until now (Contini 2017, 2016a, 2015 and references therein) are summarised in Fig. 1 (top diagram), where the distribution of the N/O abundance ratios calculated for different types of host galaxies are shown as function of the redshift. We distinguish grossly four main types: SN hosts, LGRB hosts and galaxies which were classified as SB or as AGN + LINERs according to their line intensity ratios. We would like to investigate whether the N/O wavy trend in Fig. 1 is determined by the behaviour of O/H, of N/H or else, as function of z . Although some interesting features appear in Fig. 1, to undertake a more detailed examination of the N/O distribution on z , in this paper we extend our investigation to galaxies at lower z by adding other samples e.g. those relative to HII complexes in "nearby" galaxies presented by Marino et al (2013) and in numerous low-luminosity spirals and dwarf irregular galaxies at local distances observed by Berg et al (2012). Their infrared (IR) luminosity ranges from -13 to -21.7 mag. We also added selected AGN spectra at $z \leq 0.1$ from Koski (1978, for Seyfert 2 galaxies), Cohen (1983), Kraemer et al (1994) and Dopita et al (2015) and the spectra of TypeIa SN hosts at $z \leq 0.03$ reported by Gallagher et al (2005). Moreover, we will explore star evolution in the host galaxies, considering the N/O distribution as function of metallicity (in term of the O/H relative abundance) on the basis of Henry et al (2000), MC02, etc. theories. MC02 claim that at a given metallicity the N/O ratio shows a large dispersion at low as

well as at high metallicity, not only due to the abundance determination, but principally to galaxy evolution models. We will compare our results with their models in order to obtain some information about the star characteristics throughout SN and GRB hosts.

In Sect. 2 we briefly present the spectral line calculation method and the results of modelling the samples of HII region, AGN observed line ratios and Type Ia SN host spectra. In Sect. 3 we examine the distribution of N/O versus z considering previous and new results. In Sect. 4 the N/O versus $\log(O/H)+12$ trends are investigated on the basis of the results of chemical evolution models calculated to "constrain the mode and the history of star formation in starburst galaxies" by MC02. Concluding remarks follow in Sect. 5.

2 MODELLING THE SPECTRA

Metallicities obtained for galaxies in surveys at different redshifts were calculated (see Contini 2016a,b, 2015, 2014 and references therein) by the detailed modelling of the spectral lines in the UV - optical - near IR range. Generally, the strongest lines are [OII]3727+3729 (hereafter [OII]3727+), [OIII]5007+ 4959 (hereafter [OIII]5007+) and [NII]6584+6548 (hereafter [NII]6584+) together with $H\beta$ and $H\alpha$. The [OIII]4363 line, which plays a dominant role in the modelling process (see Contini 2016b), is weak and not always available. Some spectra contain also [NeIII]3869, [SII]6717, [SII]6731 and in a few cases He, Fe and Ar lines (e.g. Hammer et al 2006).

2.1 Line intensity calculation

We use composite models which account for the coupled effect of photoionization and shocks because most galaxies at high and low redshifts are the product of merging. Photoionization and heating by a radiation source and collisional process due to shocks are used in the calculation of the line fluxes. The code SUMA is adopted. The main physical properties of the emitting gas and the element abundances are accounted for. The input parameters such as the shock velocity V_s , the atomic preshock density n_0 and the preshock magnetic field B_0 (for all models $B_0=10^{-4}$ Gauss is adopted) define the hydrodynamical field. They are used in the calculations of the Rankine-Hugoniot equations at the shock front and downstream and are combined in the compression equation which is resolved throughout each slab of gas in order to obtain the density profile downstream. The input parameters that represent the primary radiation from the SB are the effective temperature T_* and the ionization parameter U . A pure black body radiation referring to T_* is a poor approximation for a SB, even adopting a dominant spectral type (see Rigby & Rieke 2004). However, the line ratios that are used to indicate T_* , also depend on metallicity, electron temperature, density, ionization parameter, the morphology of the ionized clouds, and in particular, they depend on the hydrodynamical field. For an AGN, the primary radiation is the power-law radiation flux from the active centre F in number of photons $\text{cm}^{-2} \text{s}^{-1} \text{eV}^{-1}$ at the Lyman limit and spectral indices $\alpha_{UV}=-1.5$ and $\alpha_X=-0.7$. The primary radiation source is independent but it affects

the surrounding gas. The region surrounding the radiation source is not considered as a unique cloud, but as an ensemble of slabs with different thickness. The secondary diffuse radiation is emitted from the slabs of gas heated by the radiation flux reaching the gas and collisionally by the shock. Primary and secondary radiation are calculated by radiation transfer throughout the slabs downstream. In our model the line emitting region throughout the galaxy covers an ensemble of fragmented clouds. The geometrical thickness of the clouds is an input parameter of the code (D) which is calculated consistently with the physical conditions and element abundances of the emitting gas. The fractional abundances of the ions are calculated resolving the ionization equations for each element (H, He, C, N, O, Ne, Mg, Si, S, Ar, Cl, Fe) in each ionization level. Then, the calculated line ratios are compared with the observed ones. The calculation process is repeated changing the input parameters until the observed data are reproduced by model results, within 10 percent for the strongest line ratios and within 50 percent for the weakest ones. When the data are available, the models are also constrained by the fit of the continuum spectral energy distribution (SED).

In our previous investigations (Contini 2017, 2016a and references therein) the number of objects selected from the different surveys was relatively small because only the line spectra showing enough significant observed line ratios constraining the modelling process were considered. In the optical domain, they are [OII]3727+/ $H\beta$, [OIII]5007+/ $H\beta$, [NII]6584+/ $H\beta$ and $H\alpha/H\beta$. The $H\alpha/H\beta$ line ratios are used to correct the observed data for reddening. The [OII]/[OIII] corrected line ratios are used to determine the physical parameters characteristic of the host galaxies, i.e. the photoionizing source and, in particular, the O/H relative abundances, because oxygen is a strong coolant and affects the cooling rate of the gas in the recombination regions downstream of ionization and shock fronts. [NII]/ $H\beta$ and [SII]/ $H\beta$ are used to calculate N/H and S/H, respectively. Sometimes the observed $H\alpha/H\beta$ are relatively high (>4). They can be found in high density gas ($> 10^6 \text{cm}^{-3}$) where self-absorption occurs in the Balmer lines (Osterbrock 1974). This leads to the strengthening of the $H\alpha$ relatively to the other lines of the Balmer series (see also Contini 2003). Shock waves which are accounted for in the SUMA calculations compress the gas downstream to $n/n_0 > 4$ (the adiabatic jump) depending on V_s . Unfortunately $H\gamma$ lines are weak and often blended with [OIII]4363 line. The observation error could reach values > 50 percent. Therefore, $H\gamma/H\beta$ cannot be used to interpret the spectra properly. Therefore, before correcting the line ratios for reddening, the forbidden lines, in particular [OII] and [SII], are checked because the critical densities for collisional deexcitation are $\geq 4 \times 10^3 \text{cm}^{-3}$, while for the [OIII]5007+ lines it is $\sim 6.5 \times 10^5 \text{cm}^{-3}$. High density gas in the host galaxy can be revealed by relatively strong permitted lines and abnormally low forbidden ones. Alternatively, considering that the line fluxes are affected by gas and dust throughout their way to Earth, the data are reddened corrected by the $H\alpha/H\beta$ (case B) even implying errors within 20 percent.

The calculations by the code SUMA adopt an initial set of parameters suggested by the observation evidence. By the detailed modelling method, the O/H and N/H relative abundances are calculated consistently with the other ele-

Table 1. Modelling line ratios to $H\beta = 1$ from the CALIFA HII regions (Marino et al 2013)

ID	z	[OII]3727+	[OIII]4363	[OIII]5007+	[NII]6583	$F_{H\beta}^1$
MCG-01-54-016-001	0.0098	3.83	0.041	3.11	0.12	139.78
mc1		3.94	0.024	3.2	0.14	
NGC 3991-001	0.010	2.88	0.018	2.73	0.24	1859.3
mc2		2.8	0.017	2.85	0.25	
NGC 3991-002		3.98	0.016	2.18	0.30	1019.1
mc3		3.96	0.023	2.3	0.35	
NGC 3991-007		5.18	0.013	1.77	0.37	233.58
mc4		5.	0.03	1.87	0.33	
NGC 7489-002	0.0208	3.35	0.043	3.19	0.26	87.13
mc5		3.6	0.025	3.16	0.26	
NGC 7489-007		3.87	0.08	3.87	0.26	80.43
mc6		3.99	0.043	3.83	0.36	
UGC 00312-001	0.01456	3.51	0.015	2.93	0.23	512.98
mc7		3.6	0.02	2.91	0.25	
UGC 00312-004		3.07	0.016	2.68	0.25	296.63
mc8		3.18	0.019	2.66	0.24	
UGC 00312-005		3.97	0.018	2.38	0.26	155.21
mc9		3.7	0.021	2.33	0.25	
UGC 00312-007		3.65	0.018	2.82	0.24	155.22
mc10		3.5	0.021	2.8	0.25	
UGC 00312-008		3.0	0.034	3.12	0.19	59.91
mc11		3.2	0.022	3.15	0.2	
UGC 00312-013		4.33	0.033	1.92	0.29	39.53
mc12		4.48	0.031	1.8	0.26	
UGC 8733-004	0.0078	2.44	0.021	2.25	0.26	46.46
mc13		2.5	0.017	2.32	0.25	
UGC 10331-004	0.0149	5.78	0.019	2.12	0.39	98.87
mc14		5.3	0.023	2.17	0.4	
UGC 10796-001	0.0103	3.14	0.032	1.91	0.32	94.54
mc15		3.3	0.022	1.87	0.3	
UGC 12494-001	0.014	2.51	0.064	4.67	0.12	74.13
mc16		2.8	0.041	4.99	0.124	

¹ in 10^{-16} erg cm^{-2} s^{-1} **Table 2.** Models used to reproduce the spectra presented in Table 2

model	V_s km s^{-1}	n_0 cm^{-3}	D 10^{18}cm	N/H 10^{-4}	O/H 10^{-4}	T_* 10^4K	U -	$H\beta$ ¹ $\text{erg cm}^{-2} \text{s}^{-1}$
mc1	100	120	0.7	0.08	6.0	8.3	0.009	0.008
mc2	100	120	0.6	0.2	6.6	6.6	0.016	0.011
mc3	100	120	0.6	0.2	6.4	7.4	0.0072	0.007
mc4	100	100	0.7	0.15	6.2	8.2	0.004	0.0038
mc5	100	60	0.6	0.2	6.8	7.3	0.01	0.0035
mc6 ²	200	100	0.093	0.2	6.3	7.8	0.015	0.0137
mc7	100	100	1.0	0.18	6.2	7.4	0.0075	0.0062
mc8	100	100	1.5	0.16	6.3	7.8	0.0095	0.0077
mc9	100	100	1.5	0.15	6.5	8.1	0.006	0.0063
mc10	100	100	1.5	0.16	6.5	8.2	0.0085	0.0072
mc11	90	70	2.6	0.14	6.2	8.6	0.0085	0.0046
mc12	100	70	2.2	0.15	6.9	8.6	0.0036	0.003
mc13	100	70	5.4	0.2	6.3	8.8	0.0082	0.0063
mc14	90	170	1.8	0.16	6.6	11.	0.004	0.0093
mc15	100	67	3.4	0.2	6.6	8.3	0.005	0.0039
mc16	100	70	0.19	0.12	6.0	7.5	0.012	0.0037

¹ calculated at the nebula ; ² calculated by inflow.

Table 3. Modelling line ratios to $H\beta = 1$ from the Berg et al (2012) sample

ID	z	[OII] ₁	[NeIII] ₂	H γ ₃	[OIII] ₄	[OIII] ₅	HeI ₆	[SIII] ₇	[OI] ₈	[NII] ₉	H α ₁₀	[SII] ₁₁	[SII] ₁₂
NGC521A	0.0022	1.59	0.67	0.48	0.09	4.85	0.08	0.03	0.03	0.05	2.77	0.11	0.07
mb1		1.67	0.34	0.46	0.15	4.76	0.16	0.03	0.001	0.08	3.	0.07	0.04
UGC695E	0.00209	3.25	0.55	0.53	0.04	2.16	0.10	0.	0.1	0.16	2.86	0.43	0.27
mb2		3.0	0.43	0.46	0.02	2.4	0.25	0.	0.3	0.17	3.	0.55	0.46
UGB1056A	0.00198	3.32	0.64	0.49	0.04	3.13	0.13	0.	0.09	0.19	3.	0.4	0.31
mb3		3.2	0.77	0.46	0.022	3.3	0.2	0.	0.24	0.18	3.	0.44	0.4
UGB1056B	0.00198	2.8	0.84	0.50	0.04	4.36	0.11	0.02	0.17	0.16	2.82	0.26	0.17
mb4		2.71	0.8	0.46	0.022	4.3	0.19	0.	0.2	0.17	2.96	0.29	0.27
UGC1176A	0.0021	2.27	0.87	0.46	0.05	4.81	0.097	0.019	0.1	0.154	2.82	0.17	0.12
mb5		2.5	0.78	0.46	0.022	4.76	0.18	0.0	0.18	0.155	2.96	0.14	0.13
UGC784A	0.0007	2.19	0.53	0.46	0.05	5.5	0.11	0.02	0.073	0.145	2.89	0.2	0.15
mb6		2.3	0.83	0.46	0.023	5.54	0.17	0.0	0.17	0.14	2.9	0.19	0.18
NGC784B	0.0007	2.61	0.8	0.48	0.05	4.44	0.095	0.015	0.047	0.1	2.81	0.2	0.15
mb7		2.6	0.75	0.46	0.02	4.47	0.18	0.0	0.19	0.11	2.96	0.18	0.17
UGC2716A	0.00137	2.08	0.7	0.51	0.06	5.69	0.11	0.022	0.045	0.123	2.86	0.2	0.14
mb8		2.2	0.8	0.46	0.023	5.8	0.14	0.001	0.1	0.12	2.9	0.18	0.16
NGC2537A	0.0014	3.42	0.45	0.47	0.012	2.85	0.12	0.016	0.058	0.63	2.87	0.36	0.27
mb9		3.5	0.43	0.46	0.036	3.0	0.15	-	0.08	0.7	3.	0.37	0.34
NGC2537B	0.0014	2.79	0.26	0.44	0.016	2.38	0.11	0.013	0.025	0.54	2.79	0.26	0.18
mb10		2.99	0.36	0.46	0.03	2.6	0.16	0.001	0.06	0.6	2.98	0.33	0.3
UGC4278B	0.0018	2.03	0.6	0.46	0.033	2.54	0.08	0.013	0.038	0.08	2.8	0.18	0.13
mb11		1.83	0.3	0.46	0.032	2.67	0.16	0.01	0.024	0.09	3.	0.17	0.16
UGC4278A	0.0018	1.68	0.43	0.44	0.046	3.36	0.1	0.013	0.031	0.071	2.86	0.14	0.10
mb12		1.56	0.34	0.45	0.032	3.44	0.16	0.01	0.02	0.073	3.	0.14	0.13
NGC2552A	0.00175	2.39	0.75	0.47	0.021	3.88	0.10	0.015	0.05	0.32	2.86	0.34	0.25
mb13		2.2	0.4	0.46	0.03	3.8	0.16	0.019	0.04	0.32	3.	0.37	0.34
UGC4393B	0.0071	2.6	0.66	0.47	0.034	4.38	0.12	0.011	0.07	0.39	2.86	0.28	0.19
mb14		2.9	0.54	0.46	0.04	4.5	0.158	0.01	0.05	0.4	3.	0.23	0.21
UGC4393C	0.0071	4.06	0.5	0.48	0.036	3.45	0.11	0.017	0.11	0.4	2.87	0.39	0.28
mb15		4.0	0.44	0.46	0.044	3.68	0.15	0.014	0.06	0.5	2.96	0.26	0.22
CGCG0035-007A	0.0019	4.00	-	0.46	0.06	2.71	0.079	-	-	0.27	2.87	0.49	0.33
mb16		4.2	-	0.46	0.06	2.68	0.16	-	-	0.27	2.96	0.5	0.46
UGC5139A	0.00046	1.88	0.54	0.48	0.051	4.9	-	0.02	0.1	0.09	2.83	0.14	0.09
mb17		1.7	0.44	0.45	0.049	4.9	0.16	0.01	0.021	0.097	3.	0.14	0.13
IC559	0.0018	3.12	0.54	0.45	0.028	3.73	0.09	-	-	0.18	2.86	0.35	0.23
mb18		2.9	0.45	0.46	0.044	3.7	0.15	-	-	0.17	2.98	0.3	0.28
NGC5272A	0.0017	1.06	0.56	0.46	0.083	6.60	0.1	0.02	0.017	0.045	2.83	0.08	0.05
mb19		1.3	0.58	0.45	0.07	6.6	0.16	0.014	0.011	0.06	3.	0.13	0.12
NGC5340A	0.000017	0.58	0.61	0.47	0.06	2.53	0.09	-	-	0.016	2.81	0.05	0.05
mb20		0.54	0.36	0.46	0.03	2.62	0.17	-	-	0.015	3.1	0.06	0.05
UGC5423A	0.00116	2.08	0.6	0.46	0.07	4.65	0.1	0.02	0.1	0.15	2.86	0.31	0.22
mb21		2.2	0.5	0.46	0.044	4.55	0.15	0.02	0.03	0.18	3.	0.33	0.32
UGC5423B	0.00116	1.78	0.78	0.46	0.07	4.95	0.11	0.02	0.03	0.11	2.86	0.15	0.11
mb22		1.79	0.6	0.46	0.042	5.0	0.16	0.02	0.02	0.14	3.	0.2	0.19
NGC5672A	0.023	3.28	0.39	0.42	0.04	3.36	0.11	-	0.04	0.35	2.87	0.31	0.22
mb23		3.0	0.39	0.46	0.04	3.7	0.16	0.015	0.035	0.38	2.98	0.26	0.22
UGC5692A	0.00019	2.47	0.21	0.54	0.06	2.27	0.14	-	-	0.48	2.79	0.61	0.4
mb24		2.37	0.27	0.46	0.03	2.36	0.16	-	-	0.43	3.	0.4	0.39
UGC5797A	0.0024	1.59	0.84	0.47	0.09	7.38	0.09	0.02	0.1	0.12	2.84	0.22	0.15
mb25		1.5	0.64	0.45	0.12	7.45	0.16	0.025	0.004	0.1	3.1	0.11	0.1
UGC5923A	0.00237	4.06	0.44	0.51	0.06	3.32	-	0.02	0.08	0.31	2.78	0.31	0.22
mb26		4.4	0.54	0.46	0.052	3.4	0.16	0.02	0.18	0.27	2.96	0.37	0.31
NGC3741A	0.000764	1.6	0.73	0.46	0.06	3.78	0.1	0.018	0.026	0.068	2.83	0.12	0.09
mb27		1.8	0.6	0.45	0.031	3.64	0.16	0.01	0.021	0.09	3.1	0.13	0.12
NGC3738A	0.00076	2.91	0.67	0.47	0.03	3.94	0.12	0.02	0.07	0.25	2.83	0.32	0.23
mb28		3.1	0.5	0.46	0.039	3.82	0.16	0.013	0.056	0.2	3.	0.24	0.22
NGC3738B	0.00076	3.45	0.55	0.46	0.04	4.14	0.15	-	0.08	0.26	2.82	0.29	0.21
mb29		3.5	0.54	0.46	0.044	4.29	0.15	0.014	0.063	0.3	2.97	0.27	0.24
UGC6817	0.0008	0.94	0.78	0.46	0.068	3.86	0.1	0.015	0.019	0.038	2.83	0.07	0.05
mb30		0.98	0.58	0.45	0.04	3.9	0.17	0.007	0.01	0.06	3.1	0.08	0.07

¹ 3727+ ; ² 3869+ ; ³ 4340 ; ⁴ 4363 ; ⁵ 5007+ ; ⁶ 5876 ; ⁷ 6312 ; ⁸ 6300+ ; ⁹ 6548+ ; ¹⁰ 6563 ; ¹¹ 6717 ; ¹² 6731 ;

Table 3 - continued

ID	z	[OII] 1	[NeIII] 2	H γ 3	[OIII] 4	[OIII] 5	HeI 6	[SIII] 7	[OI] 8	[NII] 9	H α 10	[SII] 11	[SII] 12
UGC6900A	0.00197	4.13	-	0.55	-	0.83	-	-	0.3	0.68	2.83	1.11	0.6
mb31		4.1	-	0.45	-	0.88	-	-	0.5	0.66	3.	1.0	1.5
NGC4163A	0.00055	3.72	-	0.31	0.014	0.67	0.10	-	0.07	0.02	2.79	-	-
mb32		3.98	-	0.45	0.05	0.6	0.014	0.003	0.4	0.2	3.	-	-
CGCG269049C	0.00053	1.76	-	0.29	0.05	2.05	-	-	-	0.02	2.79	-	-
mb33		1.5	-	0.45	0.02	2.0	-	-	-	0.02	3.	-	-
CGCG269049A	0.00055	1.0	0.64	0.46	0.062	3.35	0.097	0.012	0.011	0.043	2.83	0.06	0.05
mb34		0.8	0.5	0.45	0.04	3.58	0.17	0.005	0.008	0.04	3.1	0.06	0.05
UGC7577A	0.00065	1.65	0.81	0.47	0.08	7.0	0.11	-	-	0.12	2.79	0.2	0.15
mb35		1.9	0.98	0.46	0.063	7.09	0.15	-	-	0.13	2.98	0.21	0.21
NGC4449C	0.00069	3.26	0.38	0.45	0.02	3.0	0.12	0.014	0.095	0.3	2.84	0.35	0.25
mb36		3.0	0.39	0.45	0.036	3.16	0.16	0.012	0.044	0.2	2.99	0.22	0.2
NGC4449B	0.00069	3.0	0.36	0.48	0.02	3.38	0.106	0.012	0.065	0.28	2.86	0.28	0.2
mb37		3.0	0.39	0.46	0.036	3.25	0.16	0.012	0.05	0.25	2.99	0.22	0.2
NGC449A	0.00069	2.4	0.42	0.47	0.019	4.61	0.11	0.014	0.037	0.211	2.83	0.18	0.13
mb38		2.7	0.49	0.46	0.04	4.4	0.157	0.013	0.22	0.22	2.99	0.21	0.18
UGC7605	0.001	1.91	0.36	0.46	0.04	3.09	0.07	0.01	0.05	0.081	2.83	0.15	0.09
mb39		1.8	0.3	0.45	0.033	3.03	0.16	0.01	0.02	0.1	3.	0.19	0.16
UGC7639A	0.00127	3.98	-	0.44	0.05	2.81	-	-	0.09	0.28	2.83	0.45	0.28
mb40		4.0	-	0.46	0.05	2.5	-	-	0.1	0.25	2.98	0.5	0.4
NGC4656A	0.00216	0.8	0.79	0.45	0.09	9.	-	0.03	0.03	0.032	2.86	0.07	0.04
mb41		1.6	0.8	0.45	0.1	8.9	-	0.01	0.02	0.06	3.	0.1	0.1
UGC8201A	0.0001	1.62	0.44	0.47	0.05	3.93	0.11	0.02	0.1	0.04	2.81	0.1	0.07
mb42		1.75	0.42	0.45	0.033	3.89	0.16	0.01	0.016	0.04	3.1	0.1	0.1
UGC8245A	0.00023	2.81	-	0.41	0.03	1.68	0.10	-	0.23	0.16	2.83	0.27	0.18
mb43		2.73	-	0.45	0.05	1.77	0.16	-	0.08	0.18	3.	0.04	0.37
UGC8508A	0.000207	1.47	0.78	0.45	0.06	4.33	0.10	0.02	0.06	0.05	2.83	0.12	0.08
mb44		1.47	0.5	0.45	0.034	4.3	0.16	0.01	0.014	0.05	3.	0.11	0.1
UGC8638A	0.000915	1.77	0.9	0.45	0.055	5.56	0.10	0.02	0.06	0.05	2.83	0.12	0.08
mb45		1.9	0.8	0.45	0.05	5.7	0.1	0.01	0.02	0.04	3.	0.13	0.12
UGC8638B	0.000915	1.75	0.34	0.47	0.06	5.54	0.11	0.018	0.017	0.08	2.81	0.11	0.09
mb46		1.75	0.5	0.45	0.053	5.8	0.016	0.012	0.017	0.09	3.	0.12	0.11
UGC8837A	0.00048	3.46	0.23	0.47	0.019	1.68	0.091	0.018	0.064	0.269	2.83	0.35	0.25
mb47		3.3	0.35	0.45	0.06	1.66	0.17	0.01	0.128	0.21	3.	0.37	0.32
NGC5477A	0.001	1.31	0.66	0.47	0.06	6.19	0.11	0.02	0.064	0.062	2.84	0.08	0.06
mb48		1.23	0.58	0.45	0.07	6.37	0.158	0.01	0.01	0.08	3.	0.1	0.1
UGC9405A	0.00074	3.66	-	0.35	-	1.9	-	-	-	-	2.79	0.79	0.55
mb49		3.6	-	0.46	-	2.2	-	-	-	-	2.98	0.5	0.45
UGC10818A	0.03	2.73	0.48	0.45	0.02	2.96	0.10	0.01	0.08	0.33	2.79	-	-
mb50		2.8	0.46	0.46	0.04	3.91	0.16	0.01	0.05	0.27	3.	-	-
KKH098A	0.0004	1.85	0.3	0.58	-	2.54	0.08	-	-	0.12	2.79	0.15	0.10
mb51		1.64	0.29	0.45	0.028	2.6	0.16	-	-	0.16	3.	0.15	0.13

¹ 3727+ ; ² 3869+ ; ³ 4340 ; ⁴ 4363 ; ⁵ 5007+ ; ⁶ 5876 ; ⁷ 6312 ; ⁸ 6300+ ; ⁹ 6548+ ; ¹⁰ 6563 ; ¹¹ 6717 ; ¹² 6731 ;

ments included in the line spectrum. This means that model parameters are selected cross-checking calculated with observed line ratios until a fine tune is obtained for all of them. Using the detailed modelling of the line spectra observed from SN and GRB hosts in our previous works, we have generally obtained O/H relative abundances higher than those found adopting strong-line direct methods. Higher O/H were justified by theoretical arguments considering that the electron temperature and density of the emitting gas throughout the host galaxy are not constant, but decrease with gas recombination. Moreover, the data are observed at Earth but calculated at the emitting nebula. The observations for nearly all the objects are averaged over the whole galaxy, so a perfect fit of the spectral line ratios is not realistic. Special features are often lost.

2.2 Models for HII region spectra

HII regions are common near very hot young stars. WD stars have temperatures close to $2 \cdot 10^5$ K. In Table 1 the modelling of Marino et al (2013) spectra from galaxies hosting HII regions are presented. Marino et al observations were obtained with the Calar Alto Legacy Integral Field Area (Califa) by using the Potsdam Multi Aperture Spectrograph (PMAS) at CAHA 3.5 m. In Table 1 the redshift is shown in column 2, followed by the observed line ratios to H β in columns 3-6. The observed flux in 10^{-16} erg cm $^{-2}$ s $^{-1}$ appears in the last column. Each row containing the data is followed by a row containing calculation results by models mc1-mc16, which are described in Table 2. All the models refer to outflowing matter, except for galaxy NGC7489-007 spectrum which required an inflow model.

Berg et al (2012) MMT spectroscopic observations of

Table 4. Models used to reproduce the spectra presented in Table 3

model	V_s km s^{-1}	n_0 cm^{-3}	D 10^{18}cm	N/H 10^{-4}	O/H 10^{-4}	Ne/H 10^{-4}	S/H 10^{-4}	T_* 10^4 K	U -	$H\beta^1$ $\text{erg cm}^{-2} \text{ s}^{-1}$
mb1	40	100	0.05	0.2	6.6	1.	0.23	4.4	0.07	4.e-4
mb2	100	60	7.	0.08	6.	1.	0.05	8.6	0.005	0.0045
mb3	100	80	2.	0.06	4.	1.	0.03	8.7	0.007	0.005
mb4	100	80	2.	0.07	4.	1.	0.02	8.3	0.012	0.007
mb5	100	80	2.	0.07	4.2	1.	0.01	8.	0.016	0.0077
mb6	100	80	2.	0.07	4.2	1.	0.013	8.	0.024	0.009
mb7	100	80	2.	0.05	4.2	1.	0.013	8.	0.014	0.0073
mb8	100	70	0.4	0.07	4.2	1.	0.013	7.	0.03	0.007
mb9	130	60	0.3	0.25	4.6	0.7	0.1	8.6	0.005	0.0035
mb10	130	60	0.35	0.25	4.6	0.7	0.1	8.6	0.005	0.004
mb11	130	60	0.58	0.07	5.3	1.	0.1	8.6	0.007	0.0063
mb12	130	60	0.71	0.07	6.6	1.	0.1	8.9	0.01	0.01
mb13	130	60	0.51	0.22	6.8	1.	0.2	8.9	0.0086	0.007
mb14	130	60	0.53	0.22	6.3	1.	0.1	9.1	0.0086	0.0068
mb15	100	60	0.42	0.22	6.6	1.	0.1	6.6	0.005	0.003
mb16	100	60	0.3	0.1	6.6	1.	0.15	7.6	0.003	0.002
mb17	130	60	0.82	0.09	6.8	1.	0.1	9.3	0.014	0.012
mb18	130	60	0.42	0.09	6.8	1.	0.13	9.3	0.006	0.0045
mb19	120	60	1.16	0.07	6.5	1.	0.13	8.3	0.025	0.015
mb20	100	60	2.14	0.07	6.6	1.6	0.13	8.9	0.016	0.02
mb21	130	70	0.39	0.12	6.5	1.	0.2	8.4	0.0096	0.0067
mb22	130	70	0.54	0.12	6.7	1.	0.15	8.4	0.015	0.012
mb23	100	50	0.69	0.22	6.6	1.	0.13	6.7	0.006	0.003
mb24	100	80	0.32	0.28	6.6	1.	0.23	6.7	0.0058	0.0058
mb25	100	65	1.45	0.13	6.2	1.	0.25	5.2	0.032	0.017
mb26	100	60	0.37	0.1	6.3	1.	0.1	8.	0.0036	0.0024
mb27	100	70	0.74	0.08	6.6	1.7	0.1	8.	0.009	0.009
mb28	100	70	0.47	0.1	6.3	1.	0.1	8.	0.0058	0.0052
mb29	100	70	0.41	0.15	6.3	1.	0.1	8.	0.0058	0.0046
mb30	100	50	1.85	0.1	6.6	1.7	0.1	8.9	0.012	0.0092
mb31	120	350	0.091	0.1	3.8	1.	0.06	0.7	4.e-4	0.0056
mb32	120	350	0.084	0.1	4.	1.	0.06	0.7	5.e-4	0.0085
mb33	100	70	0.65	0.07	6.6	1.0	0.13	6.8	0.007	0.0086
mb34	100	70	1.75	0.07	6.6	1.6	0.08	9.3	0.014	0.014
mb35	130	80	0.44	0.1	6.4	1.5	0.15	8.7	0.019	0.013
mb36	100	70	0.412	0.1	6.3	1.	0.1	7.0	0.0058	0.0049
mb37	100	70	0.411	0.13	6.4	1.	0.1	7.0	0.0058	0.0048
mb38	100	70	0.67	0.13	6.4	1.	0.1	8.0	0.0069	0.0049
mb39	100	60	0.76	0.09	6.6	1.	0.14	7.6	0.0063	0.003
mb40	100	60	0.344	0.1	6.6	1.	0.15	5.6	0.003	0.0021
mb41	130	80	0.76	0.06	6.4	1.	0.08	8.6	0.04	0.025
mb42	120	50	1.	0.09	6.8	1.2	0.1	7.1	0.012	0.0078
mb43	100	70	0.29	0.1	6.6	0.8	0.15	8.2	0.0026	0.0028
mb44	120	60	0.88	0.09	6.8	1.2	0.1	8.	0.014	0.011
mb45	120	60	0.73	0.09	6.8	1.6	0.1	8.	0.014	0.008
mb46	100	60	1.15	0.09	6.6	1.	0.1	8.	0.014	0.0093
mb47	100	60	0.3	0.1	6.6	1.	0.1	9.	0.0016	0.0016
mb48	100	70	1.2	0.1	6.4	1.	0.1	8.5	0.022	0.015
mb49	100	70	0.23	0.1	6.6	0.8	0.15	8.2	0.0023	0.0018
mb50	90	70	0.46	0.15	6.6	1.	0.1	8.4	0.004	0.0036
mb51	90	70	0.85	0.15	6.6	1.	0.1	9.9	0.005	0.0073

¹ calculated at the nebula

HII regions in 42 low luminosity galaxies with the Spitzer Space Telescope that combines IRAC and Multiband Imaging Photometer (MIPS) IR imaging for 258 galaxies in the nearest 11 Mpc of our local universe, are shown in Table 3. The observed line ratios for each galaxy are reported in columns 3-14. In the row following each dataset the results of modelling (models mb1-mb51) are given. The input parameters are shown in Table 4, where models mb1-mb51

are described. Galaxy KKH37 does not appear because the data are not sufficient to constrain the models. For all the models adopted to reproduce Berg et al data the emitting clouds are inflowing towards the starburst, as suggested by Michalowski et al (2016). This option was strengthened by the modelling of [OIII] 4363/H β line ratio, because outflowing model results underpredicted these ratios by a factor of ~ 3 . The calculated star temperatures T_* range between

Table 5. Modelling line ratios to $H\beta = 1$ of AGN spectra at $z \leq 0.1$ (Dors et al 2017)

ID	z	[OII]3727+	[OIII]5007+	[NII]6583+	[SII] 6719+	Ref
IZW92	0.038	2.63	13.5	1.3	0.77	1
ms1		2.76	13.7	1.2	0.97	
Mrk176	0.027	3.54	18.15	3.99	1.10	2
ms2		3.9	18.0	3.99	1.1	
3c33	0.0597	4.93	16.78	2.36	1.6	2
ms3		5.1	16.87	2.34	1.5	
Mrk3	0.0135	3.52	16.66	4.19	1.55	2
ms4		3.4	17.0	4.2	1.7	
Mrk573	0.0172	2.92	16.0	3.29	1.55	2
ms5		2.99	16.2	3.3	1.58	
Mrk78	0.037	4.96	15.82	3.05	1.62	2
ms6		4.74	16.	2.9	1.7	
Mrk34	0.051	3.43	15.14	2.88	1.62	2
ms7		3.7	14.8	2.9	1.5	
Mrk1	0.016	2.78	14.51	2.98	1.0	2
ms8		2.97	14.66	3.97	1.3	
3c433	0.1	6.17	12.81	7.22	2.71	2
ms9		5.5	12.9	6.9	2.9	
Mrk270	0.01	5.44	11.67	3.88	2.6	2
ms10		5.8	11.65	3.8	2.6	
3c452	0.081	4.81	9.25	4.96	1.87	2
ms11		4.83	9.27	4.9	1.6	
Mrk198	0.024	2.51	7.35	2.95	1.57	2
ms12		2.7	7.1	2.98	1.56	
Mrk268	0.04	3.75	6.37	6.41	2.36	2
ms13		3.66	6.22	6.35	2.3	
NGC3227	0.00385	3.32	14.3	6.68	2.5	3
ms14		3.1	14.7	6.8	2.5	
Mrk6	0.01	2.45	13.5	2.38	1.25	3
ms15		2.6	13.5	2.34	1.2	
NGC7590	0.0052	3.32	4.63	2.47	1.77	3
ms16		3.7	4.8	2.7	1.8	
NGC613	0.0049	2.42	0.68	2.27	0.91	4
ms17		2.2	0.7	2.39	0.8	
IC1657	0.0119	3.67	2.38	2.52	1.85	4
ms18		3.4	2.27	2.59	1.6	
IRAS1475	0.0177	1.78	6.65	2.25	0.54	4
ms19		1.9	6.68	2.3	0.65	
IC1816	0.0169	1.99	13.7	6.0	2.16	4
ms20		2.3	13.6	6.4	2.3	
NGC1125	0.0109	3.14	8.21	2.87	1.38	4
ms21		3.26	8.5	2.81	1.48	
MCG-06	0.0152	2.92	9.53	3.47	1.93	4
ms22		3.1	9.34	3.4	1.9	
IRAS11	0.014	2.46	10.49	2.16	1.34	4
ms23		3.08	10.6	2.2	1.6	
ESO137	0.0091	3.10	12.4	4.97	2.36	4
ms24		3.0	12.47	4.9	2.3	
NGC6300	0.0037	5.41	19.73	6.62	1.7	4
ms25		5.0	19.8	6.3	1.7	
ESO103	0.013	3.19	9.8	4.23	2.06	4
ms26		3.1	10.	4.3	2.	
NGC6926	0.0196	5.84	5.84	4.8	2.5	4
ms27		5.4	6.	4.87	2.5	
IC1368	0.013	4.56	4.8	4.51	1.31	4
ms28		4.5	4.8	4.4	1.24	

Ref : 1 Kraemer et al (1994) ; 2 Koski (1978); 3 Cohen (1983) ; 4 Dopita et al (2015)

Table 6. Models used to reproduce the spectra presented in Table 5

model	V_s km s^{-1}	n_0 cm^{-3}	F 2	D 10^{17}cm	N/H 10^{-4}	O/H 10^{-4}	S/H 10^{-4}	$H\beta$ (calc) ¹ $\text{erg cm}^{-2} \text{s}^{-1}$
ms1	320	330	16.	7.	0.3	5.8	0.07	0.25
ms2	120	420	10.	0.5	1.	5.7	0.036	0.1
ms3	280	200	10.	70.	0.45	6.6	0.04	0.12
ms4	190	470	37.	0.8	1.	6.6	0.1	0.33
ms5	210	470	37.	0.8	0.8	6.5	0.1	0.37
ms6	300	200	9.	80.	0.6	6.6	0.05	0.12
ms7	280	290	12.	20.	0.6	6.0	0.05	0.166
ms8	320	280	16.	0.7	0.7	5.3	0.1	0.2
ms9	210	150	1.8	1.	1.8	7.0	0.15	0.029
ms10	210	150	1.5	1.	0.9	6.6	0.12	0.026
ms11	330	180	2.4	1.	1.1	6.6	0.08	0.05
ms12	400	200	4.4	1.6	1.	6.6	0.12	0.12
ms13	380	160	2.	1.2	1.8	6.6	0.13	0.053
ms14	310	280	13.	0.7	1.8	6.6	0.19	0.19
ms15	330	330	17.	0.7	0.6	6.0	0.09	0.27
ms16	380	190	1.9	1.0	0.7	6.2	0.12	0.055
ms17	330	330	0.6	0.7	0.8	6.0	0.09	0.0295
ms18	320	320	1.5	0.7	0.6	6.6	0.012	0.048
ms19	360	360	8.4	0.7	0.8	6.6	0.07	0.26
ms20	320	370	21.	0.7	1.5	5.4	0.17	0.29
ms21	400	180	4.4	1.6	0.9	6.7	0.1	0.11
ms22	400	170	4.8	1.6	1.1	6.7	0.13	0.11
ms23	400	190	7.0	1.6	0.7	6.8	0.1	0.155
ms24	300	320	10.	0.8	1.3	6.8	0.18	0.18
ms25	100	330	4.6	0.4	2.0	7.0	0.15	0.053
ms26	400	170	5.5	1.6	1.4	6.8	0.14	0.12
ms27	380	120	0.98	1.0	1.1	6.6	0.13	0.024
ms28	380	160	1.3	1.0	1.0	6.2	0.07	0.035

¹ calculated at the nebula; ² in $10^{10} \text{ photons cm}^{-2} \text{ s}^{-1} \text{ eV}^{-1}$ at the Lyman limit;

$6.6 \times 10^4 \text{K}$ and $1.1 \times 10^5 \text{K}$ for the Marino et al spectra and between 4.4 and $9.9 \times 10^4 \text{K}$ for the Berg et al ones. The ionization parameter U is low (< 0.1) for both samples. Tables 1 and 3 and Fig. 2 diagrams show that calculated line ratios reproduce the observed ones within 10 percent for the strong lines ([OII], [OIII]5007+, [NII] and roughly for [SII]), while weak lines are reproduced by ~ 50 percent. [SIII] 6312 lines are easily blended with [OI]6300, 6363 and the [OIII]4363 line with $H\gamma$.

We compare in Fig. 3 the N/O line ratios calculated with the strong-line direct methods by Berg et al with those calculated in the present paper. The resulting trend suggests that discrepancies are in average systematic. Fig. 3 shows that the N/O ratios calculated by direct methods are shifted towards higher values, indicating that the ratios between the $(O/H)_d$ (evaluated by direct methods) are smaller than those $(O/H)_m$ (calculated by the detailed modelling).

2.3 Calculations of AGN spectra

We refer to the spectra assembled and modelled by Dors et al (2017), making use of the code CLOUDY. We have selected the galaxies corresponding to lines uncontaminated by broad components, adapted to Seyfert 2 galaxies and corrected for reddening. The observation source references are reported in Table 5, last column. The observed line ratios from the AGN sample appear in columns 3-6 of Table 5 and the best fitting results by models ms1-ms28 are given in the next row.

Observed line ratios and model results are compared in Fig. 2, which shows that the data are satisfactorily reproduced. The models are described in Table 6. Note that V_s and n_0 are higher than those calculated for HII, SB and LGRB host galaxies, similar to those in the NLR of AGN.

We can now compare in Fig. 3 the results obtained by a pure photoionization code (CLOUDY) with those calculated by a code which refers to the coupled effect of shock and photoionization (SUMA). Fig. 3 shows that the results obtained by both the pure photoionization code and by the strong-line direct method lead to N/O higher than those obtained by models accounting also for the shock. The [OIII]5007+/ $H\beta$ line ratios are reproduced by SUMA with more precision than by CLOUDY (cf Dors et al 2017, fig. 1) because Dors et al used a constant electron density N_e throughout the recombination zone, whereas by SUMA N_e decreases following the cooling rate. Our results lead to O/H close to solar for most AGNs and for most of the HII regions. We will conventionally define "solar" relative abundances $(O/H)_\odot = 6.6 - 6.7 \times 10^{-4}$ and $(N/H)_\odot = 9. \times 10^{-5}$ (Allen 1976, Grevesse & Sauval 1998) that were found suitable to local galaxy nebulae. Moreover, these values are included between those of Anders & Grevesse (1989) (8.5×10^{-4} and 1.12×10^{-4} , respectively) and Asplund et al (2009) (4.9×10^{-4} and 6.76×10^{-5} , respectively).

Table 7. Modelling line ratios to $H\beta = 1$ of TypeI SN host spectra at $z \leq 0.03$ (Gallagher et al 2005)

galaxy	SN	z	[OII]	[OIII]	[OI]	[NII]	H α	[SII]	[SIII]
NGC4536	1981B	0.006	3727+	5007+	6300	6548+	6563	6717	6731
mg1			10.7	1.0	0.16	1.7	3.	0.65	0.47
NGC3627	1989B	0.0024	1.28	0.28	0.08	1.8	3.	0.49	0.4
mg2			1.34	0.34	0.06	1.9	3.	0.35	0.36
NGC4639	1990N	0.003	16.2	1.3	0.3	0.2	3.	0.88	0.5
mg3			14.0	2.1	1.	0.4	3.	0.98	0.75
NGC4527	1991T	0.0058	6.8	1.56	0.	1.8	3.	0.43	0.42
mg4			6.7	1.33	0.3	2.0	3.	0.5	0.4
IC4232	1991U	0.031	0.24	0.4	0.09	2.2	3.	0.42	1.3
mg5			0.7	0.2	0.03	1.3	3.	0.42	0.6
Anon	1992ag	0.000	3.5	1.9	0.07	1.6	3.	1.	0.45
mg6			3.7	1.9	0.14	1.6	3.	0.6	0.5
CGCG224	1994Q	0.0295	4.1	0.5	0.11	1.	3.	0.7	0.44
mg7			4.3	0.88	0.2	1.1	3.	0.56	0.55
NGC4495	1994S	0.015	5.2	1.2	0.11	1.6	3.	0.54	0.7
mg8			5.2	1.2	0.2	1.9	3.	0.64	0.43
NGC3370	1994ae	0.0043	5.43	0.51	0.	1.3	3.	0.66	0.42
mg9			5.4	1.	0.3	1.3	3.	0.64	0.63
NGC2441	1995E	0.012	4.66	0.74	0.03	1.9	3.	0.82	0.6
mg10			4.7	0.9	0.2	2.	3.	0.65	0.64
IC1844	1995ak	0.0227	5.53	0.57	0.08	1.45	3.	0.73	0.48
mg11			5.6	1.	0.2	1.36	3.	0.67	0.65
NGC3021	1995al	0.0051	3.2	0.45	0.1	1.6	3.	0.47	0.4
mg12			3.3	0.7	0.15	1.65	3.	0.42	0.42
Anon	1996C	0.000	7.6	0.57	0.48	2.5	3.	1.1	0.66
mg13			7.5	1.2	0.9	2.7	3.	1.0	0.96
Anon	1996bl	0.000	31.	2.16	0.34	0.24	3.	0.71	0.48
mg14			26.	3.6	1.2	0.38	3.6	0.8	0.6
NGC0673	1996bo	0.0174	3.7	0.92	0.06	1.46	3.	0.59	0.49
mg15			3.8	0.8	0.2	1.6	3.	0.49	0.5
UGC03432	1996bv	0.0167	9.87	2.1	0.18	1.05	3.	0.96	0.84
mg16			9.9	2.1	0.7	1.07	3.	0.98	0.86
NGC4680	1997bp	0.0083	3.	0.4	0.3	1.66	3.	0.56	0.42
mg17			3.1	0.68	0.12	1.56	3.	0.53	0.49
Anon	1997br	0.000	4.55	2.96	0.21	1.33	3.	0.51	0.48
mg18			4.57	2.9	0.2	1.4	3.	0.53	0.5
NGC0105	1997cw	0.0176	5.6	1.98	0.1	1.7	3.	0.59	0.45
mg19			5.3	1.97	0.3	1.6	3.	0.54	0.5
UGC03845	1997do	0.01	6.69	1.4	0.076	0.98	3.	0.74	0.57
mg20			6.5	1.32	0.4	1.	3.	0.75	0.65
NGC6627	1998V	0.0176	3.44	1.55	0.096	2.5	3.	0.55	0.42
mg21			3.5	1.6	0.15	2.7	3.	0.55	0.5
NGC4704	1998ab	0.027	2.18	0.34	0.075	2.93	3.	1.47	0.4
mg22			2.1	0.45	0.06	2.7	3.1	0.8	0.7
NGC3982	1998aq	0.0037	3.3	0.79	0.07	1.56	3.	0.59	0.4
mg23			3.4	0.86	0.12	1.56	3.	0.56	0.5
UGC00139	1998dk	0.0132	3.8	0.8	0.15	1.29	3.	0.73	0.52
mg24			3.7	1.	0.15	1.2	3.	0.7	0.62
UGCA017	1998dm	0.0065	6.66	2.26	0.1	0.75	3.	0.72	0.47
mg25			6.5	2.47	0.2	0.73	3.	0.71	0.72
NGC0632	1998es	0.011	2.72	0.57	0.15	1.59	3.	0.6	0.46
mg26			2.5	0.53	0.0	1.53	3.	0.57	0.51
NGC6063	1999ac	0.0095	4.17	0.32	0.13	1.7	3.	0.68	1.
mg27			4.	0.7	0.27	1.6	3.	0.65	0.7

2.4 Models for TypeIa SN host galaxies

We present in Table 7 the modelling of TypeIa SN host galaxies at $z \leq 0.03$. The spectra reported by Gallagher et al (2005) were obtained with the FAST spectrograph (Fabricant et al 1998) at the F.L. Whipple Observatory's 1.5 m Tillinghast telescope. We have reddening corrected the

line intensity fluxes. The galaxies showing enough lines to constrain the models were selected. For some galaxies, e.g. IC3690, NGC2595 etc., the correction yields to $[OII]/H\beta \geq 80$. Such high values could be found adopting shock dominated models ($U=0$), but they would correspond to $[OIII]/H\beta > 10$. The data are far lower, therefore we omit-

Table 8. Models used to reproduce the spectra presented in Table 7

model	V_s km s ⁻¹	n_0 cm ⁻³	D 10 ¹⁸ cm	N/H 10 ⁻⁴	O/H 10 ⁻⁴	S/H 10 ⁻⁴	T_* 10 ⁴ K	U 10 ⁻³	$H\beta$ ¹ 10 ⁻³ erg cm ⁻² s ⁻¹
mg1	70	60	1.9	0.3	6.6	0.04	8.6	0.5	0.37
mg2	100	100	3.9	1.4	6.	0.15	4.6	0.5	3.3
mg3	80	60	1.2	0.06	6.2	0.03	20.	0.6	0.42
mg4	80	60	1.8	0.6	6.6	0.04	7.5	0.8	0.63
mg5	100	250	1.4	1.3	5.3	0.2	3.2	4.8	20.
mg6	70	80	0.8	0.7	6.9	0.06	6.	4.	2.4
mg7	100	100	0.8	0.4	6.4	0.06	6.	2.	2.5
mg8	100	100	0.8	0.6	6.7	0.06	7.	2.	2.5
mg9	100	100	0.8	0.4	6.6	0.06	7.	1.3	1.8
mg10	100	100	0.8	0.7	6.6	0.07	6.4	1.3	1.85
mg11	100	100	0.8	0.4	6.5	0.06	7.3	1.3	1.8
mg12	100	100	0.8	0.8	6.5	0.065	4.8	1.3	1.9
mg13	100	130	1.8	0.6	6.6	0.06	17.	1.	3.1
mg14	80	50	0.4	0.03	6.6	0.02	30.	0.8	0.29
mg15	100	130	1.8	0.6	6.6	0.06	7.6	1.3	4.1
mg16	100	80	1.	0.2	6.6	0.05	13.	1.3	1.3
mg17	100	80	1.	0.86	6.6	0.09	4.6	1.3	1.6
mg18	100	80	1.	0.5	6.6	0.045	7.5	5.	3.5
mg19	100	80	1.	0.5	6.6	0.045	7.5	3.	2.5
mg20	100	70	1.	0.3	6.6	0.06	8.2	1.	1.
mg21	100	70	1.	1.2	6.6	0.06	6.2	4.5	2.86
mg22	100	70	1.	1.8	6.6	0.16	4.2	3.3	2.3
mg23	100	70	1.	0.8	6.6	0.07	5.2	3.	2.2
mg24	100	70	1.	0.5	6.6	0.08	5.5	3.	2.2
mg25	100	70	1.	0.2	6.6	0.05	8.5	2.6	1.9
mg26	100	70	1.	0.9	6.6	0.1	4.2	2.6	2.
mg27	100	120	1.	0.6	6.6	0.08	5.9	1.3	2.5

¹ calculated at the nebula

ted them from our sample. The observed-corrected line ratios to $H\beta$ appear in Table 7. Each row which refers to the data is followed by one which shows the modelling results. The models (mg1-mg27) are presented in Table 8. Our models lead to O/H very close to solar values, similar to those found for AGN in this z range. The N/H ratios are included between solar and 0.2 solar. A few spectra (corresponding to NGC3627, IC4232, NGC6627 and NGC4704) were fitted by N/H =1.2-1.8 solar.

3 EVOLUTION OF N/O WITH Z

In the present and previous investigations the host galaxy samples were selected by the simple criterion that each spectrum contained enough lines to constrain the model, without referring to specific redshifts. Nevertheless, Fig. 1 shows that the SN and LGRB host domains do not entirely overlap throughout z . N/O ratios calculated for SN and LGRB host galaxies peak at different z and have different trends throughout the redshift. We suggest that LGRB hosts are observable at higher z because they are more luminous. In Figs. 4 and 5 the host galaxies are distinguished in subclass objects recognizable by different symbols. They refer to the different types of SN, to LGRB, SGRB and to AGN, LINER and SB galaxies, for comparison. We have added in the diagrams N/O, O/H and N/H model results presented in Tables 2 and 4 for HII region hosts calculated using the data of Marino et al (2013) and Berg et al (2012), respectively and for AGN (Table 6) and Type1a SN hosts (Table 8). Symbols

are described in Table 9. In the bottom diagrams of Figs. 4 and 5 $\log(N/H)$ and $\log(O/H)$ distributions for all type of objects are shown as function of z . Fig. 1 shows that, at the state of the art, SN and LGRB N/O domains overlap at $0.03 < z < 1$. In this z range the N/O ratios for most objects are < 0.1 (solar N/O =0.136), except for a few objects. N/O ratios in SN host band peak at a lower z (Fig. 4) than LGRB hosts (Fig. 5). In the upper panels of Figs. 4 and 5 we have added the cosmic ages corresponding to the redshifts at which significant changes occurred in the N/O trends.

3.1 SN, AGN and LINER host domains throughout the redshift

In Fig. 4, we distinguish 4 zones relative to the N/O behaviour of SN hosts and other galaxies as function of z .

1) At $z > 1.58$ (zone 1) at an age < 4.125 Gyr, we have significant data only for AGN. N/O spans between ~ 0.2 to ~ 0.015 , due to low N/H and O/H close to solar, indicating that massive stars dominate. (We adopt $(N/H)_\odot = 9. \times 10^{-5}$ and $(O/H)_\odot = 6.6 \times 10^{-4}$).

2) At $0.16 < z < 1.58$ (zone 2) at an age between 4.12 and 11.7 Gyr, N/O ratios for most SN types span between > 0.16 and < 0.01 . Both O/H and N/H extend towards ratios lower than solar by factors of ~ 10 , where the N production is primary. Intermediate mass stars appear. SLSNI and other SN types are seen throughout the N/O band of SN hosts.

3) At $0.018 < z < 0.16$ (zone 3) at an age between 11.7 and 13.47 Gyr, the N/O band of SN hosts increases rapidly to

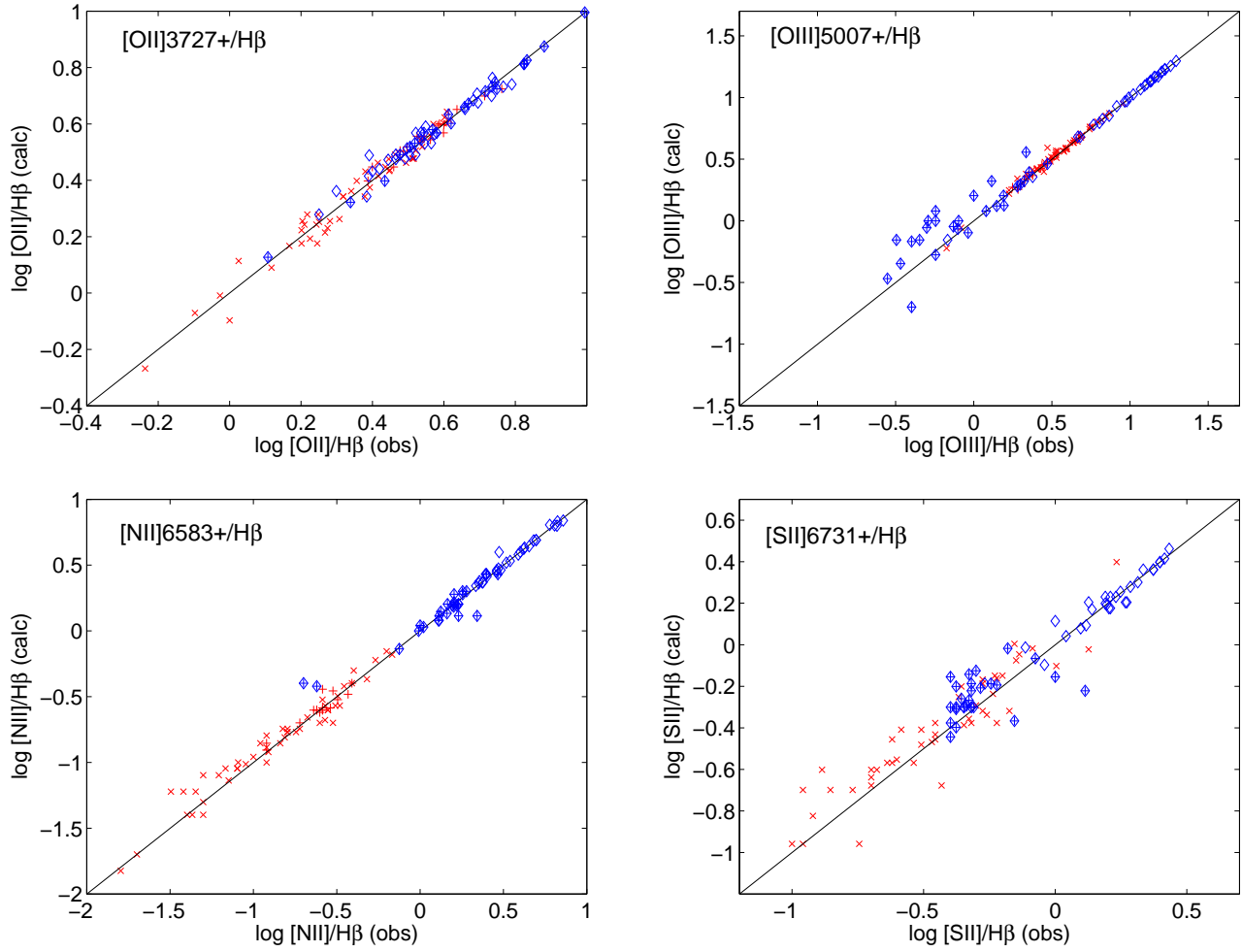


Figure 2. Observed versus calculated line ratios. Cross : Berg et al. data; plus : Marino et al data ; diamond : AGN galaxies (References in Table 5); diamond+plus : Gallagher et al data.

solar values. Both N/H and O/H reach solar values, but with different trends. Following Henry et al (2000), secondary N is created.

4) At $z < 0.018$ (zone 4) at an age > 13.48 Gyr the O/H and N/H ratios in AGN are \sim solar, reaching $N/H \sim 5 \cdot 10^{-4}$ by N secondary production at low z . The distribution of N/O data in Fig. 4 for AGN and Seyfert 2 galaxies strengthens the evidence that AGN (+LINERs) extend the N/O trend of SN hosts towards low z . SN Type 1a hosts fill the gap within the SN band (in particular in the lower edge) at low z , close to the AGN.

Summarizing, Fig. 4 shows that: N/O calculated for super-luminous SN typeIb (SLSNI, Leloudas et al. 2015) host galaxies are located at most in the lower edge of the SN band. Few super-luminous SNRI with low O/H are located on the top edge of the SN host band. SLSN hosts appear throughout a large range of N/O at $z \sim 0.1$. N/O calculated for LINERs and AGN are maximum at $z \sim 0.01$, then they split into two main trends towards lower z , following the N/H trends.

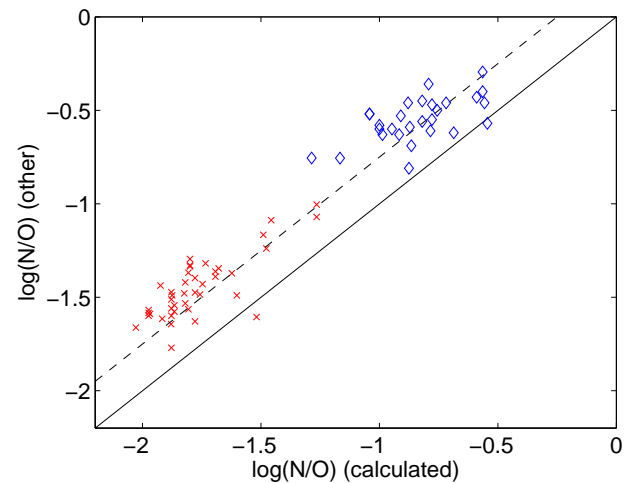


Figure 3. Comparison of N/O calculated by detailed modelling with N/O calculated by strong-line direct methods by Berg et al (2012) (cross) and with the pure photoionization code CLOUDY by Dors et al (2017) (diamond)

3.2 LGRB, SB and HII region host domains throughout the redshift

In Fig. 5, we roughly distinguish 4 zones :

1) At z between ~ 3 and ~ 0.4 (zone 1), at an age between of 2.17 and 9.4 Gyr, N/O calculated for SB are higher than for LGRB hosts, due to higher N/H and depleted O/H. Then, N production is primary. Intermediate massive stars dominate in the SB host sample. On the other hand, O/H ratios are nearly solar for LGRB hosts and N/H lower than solar (secondary N production is starting), confirming that massive stars dominate in the LGRB hosts; The primary/secondary behaviour of nitrogen was well explained by Vila-Costas & Edmunds (1993, fig. 4). SB host galaxies show a large dispersion of O/H ratios between solar and 0.24 solar.

2) At z between 0.4 and 0.158 (zone 2), at an age between 9.4 and 11.73 Gyr, a rapid fall of N/O calculated for both SB and LGRB hosts is seen also for N/H and O/H (bottom diagram). The decrease of O/H for the SB started already in zone 1. For LGRB hosts it is sharp on the upper bound distribution due to the results obtained for LGRB modelling the Niino et al (2016) survey host galaxies. The minimum at $0.1 < z < 0.4$ which corresponds to a similar minimum of N/H was explained by Contini (2017) as due to the merging process which implies inclusion of low N/H and O/H matter. The minimum at $\log(z) \sim -0.8$ corresponds to $N/O \sim 0.025$ (0.18 solar). Comparing with Contini (2017, fig. 2) at this redshift N/H shows a minimum of 10^{-5} while $O/H = 5 \cdot 10^{-4}$ is recovering from a minimum of $4.6 \cdot 10^{-4}$ at $\log(z) \geq -1$, perhaps indicating that massive stars are formed following the merging process.

3) At z between 0.158 to 0.063 (zone 3), at an age between 11.73 and 12.87 Gyr, the LGRB hosts regain solar O/H and N/H. Massive and intermediate mass stars coexist.

4) At $z < 0.063$ (zone 4) : N/H data for SB hosts seem to increase towards lower z , reaching also higher than solar values. On the other hand, the few LGRB hosts show O/H and N/H ratios merging with those calculated for the HII regions. The latter show N/H values scattered around ~ 0.1 solar and $O/H \leq \text{solar}$ (Tables 2 and 4), leading to a slowly decreasing and large spread of N/O ratios towards low z .

Summarizing, in zone 1 intermediate mass stars dominate for SB but not for LGRB, where massive stars prevail. In zone 2 both N/H and O/H decrease indicating merging. In zone 3 the poor production of secondary nitrogen leads N/H in LGRB towards ~ 0.1 solar and O/H solar, and low N/O. The lowest N/H ratios characterize SGRB host galaxies.

4 N/O VERSUS METALLICITY

We have noticed in the previous sections that, relatively to the N/O distribution, HII regions can be considered as the continuation of the LGRB host distribution at low z . Comparing the physical parameters presented in Tables 2 and 4 for HII regions with those presented for LGRB, SN and SB (Contini 2017 and references therein) slightly lower V_s , n_0 and U were found for HII regions, but similar T_* , indicating that the photoionizing source of the host galaxy

Table 9. Symbols in Figs. 4 and 5

symbol	object	Ref.
encircled dot	SLSNR hosts	(1)
triangles at $z \geq 0.1$	SLSNII hosts	(2)
filled triangles	SLSNI hosts	(3)
square+dot	SD models for SLSN hosts	(4)
square+cross	Type Ic host central	(5)
circle+cross	Type Ic host at SN positions	(6)
triangles at $z \leq 0.1$	SN Ib host	(7)
encircled triangles	SN Iib hosts	(8)
opposite triangles	SN Ic hosts	(9)
double triangles	SN IcBL hosts	(10)
hexagrams	SN Ibc	(11)
asterisks	GRB hosts	(12)
triangle+cross	LGRB hosts	(13)
pentagrams	LGRB different hosts	(14)
triangle +plus	LGRB hosts with WR stars	(15)
encircled asterisks	LGRB at low z	(16)
hexagrams (green)	SGRB hosts	(17)
diamonds	other galaxies	(18)
dots	starburst galaxies	(19,25)
circles	AGN	(20,21,25)
filled circles	LINER	(22)
plus	low-luminosity nearby galaxies	(23)
cross	HII regions in local galaxies	(24)
diamonds+plus	TypeI SN hosts	(26)

(1), (2), (3), (4) (Leloudas et al); (5), (6) (Modjaz et al); (7), (8), (9), (10), (11) (Sanders et al); (12) (Krühler et al); (13) (Savaglio et al); (14) (Contini 2016a, table 8); (15) (Han et al); (16) (Niino et al); (17) (de Ugarte Postigo et al); (18), (19), (20) (Contini 2014 and references therein); (21) (Koski 1978, Cohen 1983, Kraemer et al 1994, Dopita et al 2015; (22) (Contini 1997); (23) (Marino et al 2013); (24) (Berg et al 2012); (25) (Contini 2016b); (26) (Gallagher et al 2005).

gas is roughly the same. SB galaxies are distributed along the whole z range. However, most of them at high z show N/O ratios higher than in LGRB hosts, due to higher N/H and lower O/H ratios. It is generally considered that the SN and GRB hosts are SB dominated. However, SB and LGRB host characteristics diverge at high z . Moreover, Figs. 4 and 5 show that the N/O ratios calculated for SN and LGRB host galaxies follow roughly the trends of N/H as function of z . This indicates that N and O ejections originating from the bursts have different histories in times.

To have a wider picture of these features we now investigate whether the models calculated for the chemical evolution of starburst galaxies by MC02 could explain the behaviour of N/O as function of O/H for the different galaxy types (SN, GRB hosts and other galaxies). MC02 claim that the variation of N/O at constant metallicity may originate from a time delay between the release of oxygen and that of nitrogen in the ISM. The delayed-release model assumes that star formation is an intermittent process in galaxies and the delayed release of nitrogen produced in long lived low mass stars compared to oxygen produced in massive short-lived stars should be considered. Multi-burst scenarios were found for massive starburst nucleus galaxies.

In Figs. 6 some significant model results from the calculations of MC02 (their fig. 1) about continuous star formation and bursting star formation, are schematically overlaid upon the results obtained by the detailed modelling of the

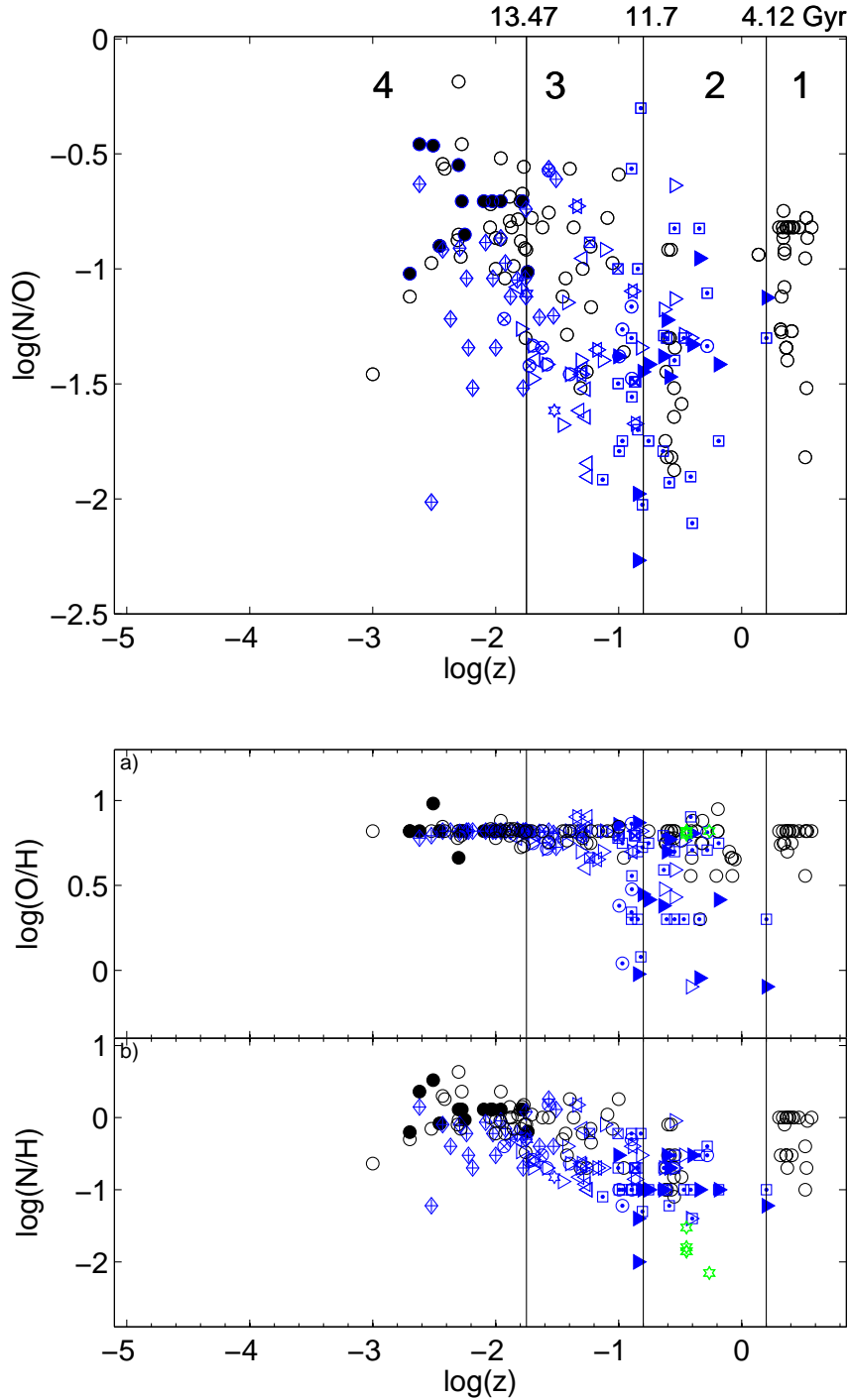


Figure 4. Top : distribution of N/O as function of the redshift for SN hosts, AGN and LINERS; bottom : distribution of O/H in 10^{-4} units and N/H in 10^{-4} units as function of the redshift for SN hosts, AGN and LINER galaxies. Symbols are explained in Table 9.

spectra in previous sections. $\log(N/O)$ is shown as function of $\log(O/H)+12$. We have reported in Fig. 6 MC02 (fig. 1, left diagram) lower and higher bounds of continuous star formation models, including the low N/O-O/H left-bottom region, by thick and thin solid lines, respectively. The models merge in the top-right region at high $\log(N/O)$ and high $\log(O/H)$. The thick-solid line in Figs. 6 refers to models with an infalling time $\tau_f = 4$ Gyr and a star forma-

tion timescale $\tau_{SF} = 2$ Gyr, while the thin line refers to $\tau_f = 7$ Gyr and $\tau_{SF} = 20$ Gyr. The dot-dashed lines circumscribe the regions of star-bursting formation models (MC02, fig. 1, right diagram) at low and high $\log(O/H)$. We report our results on the basis of Figs. 4 and 5, i.e. distinguishing between LGRB, SB and HII regions in Fig. 6 (bottom diagram) and SN and AGN hosts (top diagram). Symbols are given in Table 9. In the LGRB sample, the dichotomy noticed by

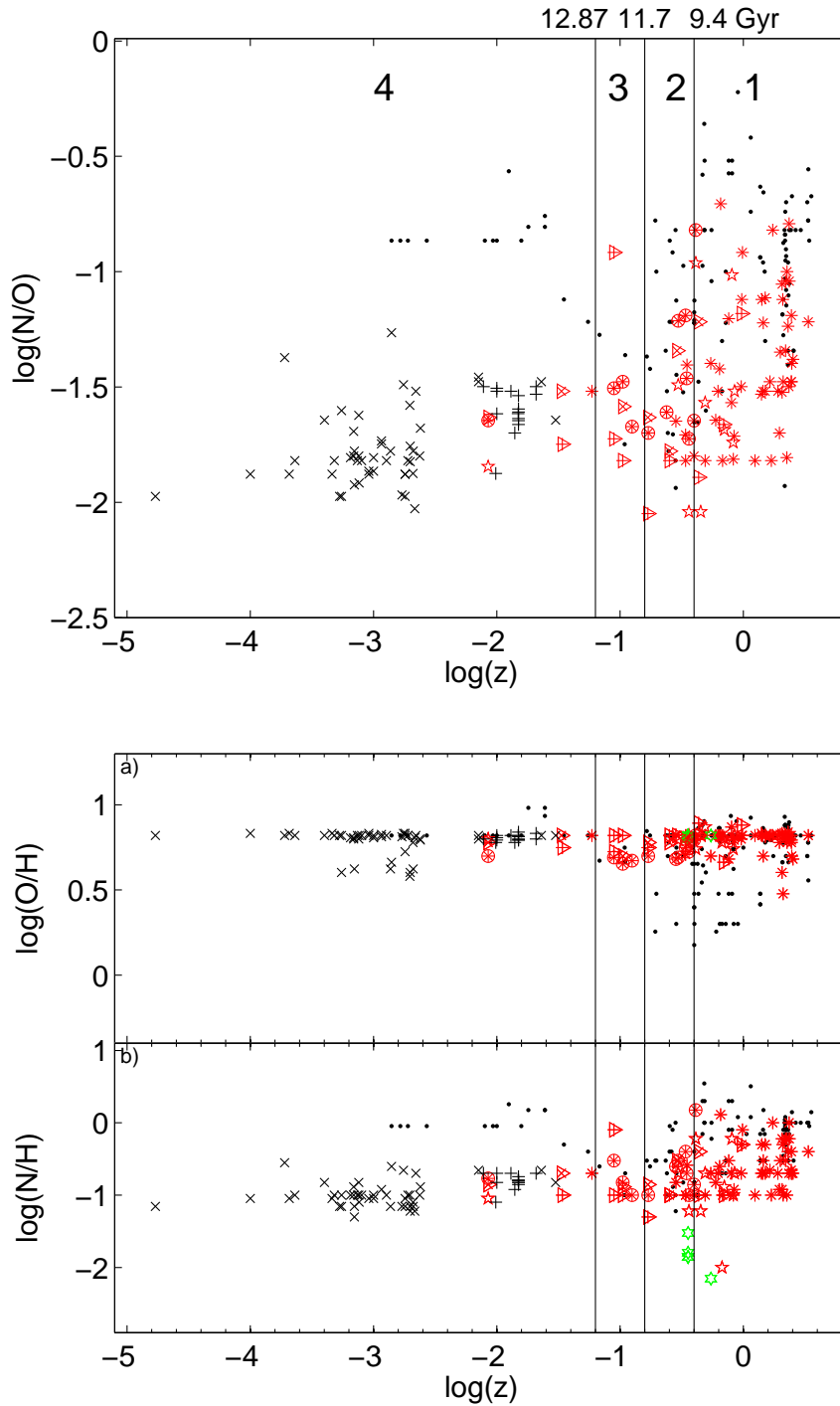


Figure 5. The same as in Fig. 4 for GRB, SB and HII region host galaxies.

MC02 between galaxies with $\log(O/H)+12$ higher or lower than 8.5, is roughly evident. Some LGRB host galaxies appear near continuous star formation models, most of them are located within the star-bursting formation domain and beyond, where also some SN hosts can be seen. The low O/H - N/O region refers mostly to dwarf irregular or metal poor UV-selected galaxies. Calculated N/O for HII region do not appear in this region. At $12+\log(O/H) > 8.6$ many different objects are nested close to O/H solar with N/O ranging

between the maximum shown by the starburst galaxies and AGN and the minimum shown by the HII regions. SGRB are located at extremely low N/O, due to low N/H. HII region and SB host galaxies splits at the same metallicity in low and high N/O, respectively.

Relatively high N/O calculated in some SN hosts, SB and AGN are explained by star-bursting models. In general, N/O in SN hosts (Fig. 6 top) do not follow MC02 model

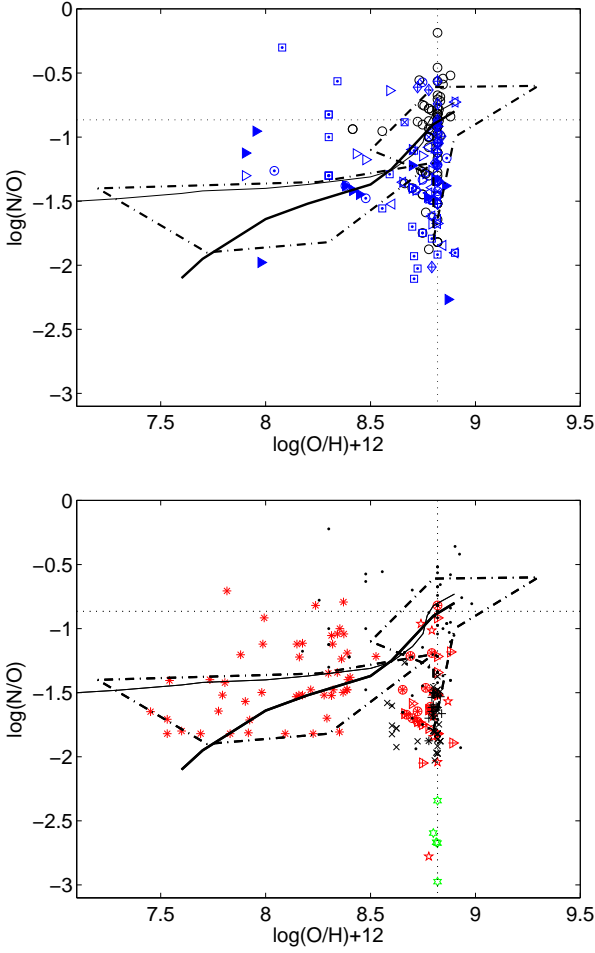


Figure 6. Top : $\log(N/O)$ versus $\log(O/H)+12$ for different types of SN and AGN host galaxies. Bottom : the same as top diagram for different types of GRB, SB and HII region host galaxies. Symbols are given in Table 9.

results at low O/H. Therefore, the SN host characteristics are different from those of the HII region and LGRB hosts.

5 CONCLUDING REMARKS

The distribution of the N/O abundance ratios over the full redshift range considered here is calculated by the detailed modelling of line spectra in order to compare the characteristic metallicities in various galaxy types, in particular SN and LGRB hosts at $z \leq 3.5$ (age ≥ 1.823 Gyr). SN and LGRB host galaxy spectra reported in this paper were selected among those showing enough significant lines to constrain the models. The available data for galaxies at $z > 3.5$ are too few to draw reliable conclusions. Our results are summarized in Fig. 7. We have found that the N/O abundance ratios calculated to fit the line ratios peak at different z , higher for LGRB than for SN hosts, depending perhaps on larger luminosities in LGRB hosts. They also show different trends as function of z .

The N/O ratios calculated in SN hosts appear within a band which increases from $z \sim 0.63$ (6 Gyr) towards $z \sim 0.01$ (13.58 Gyr), following secondary N formation. O/H rapidly

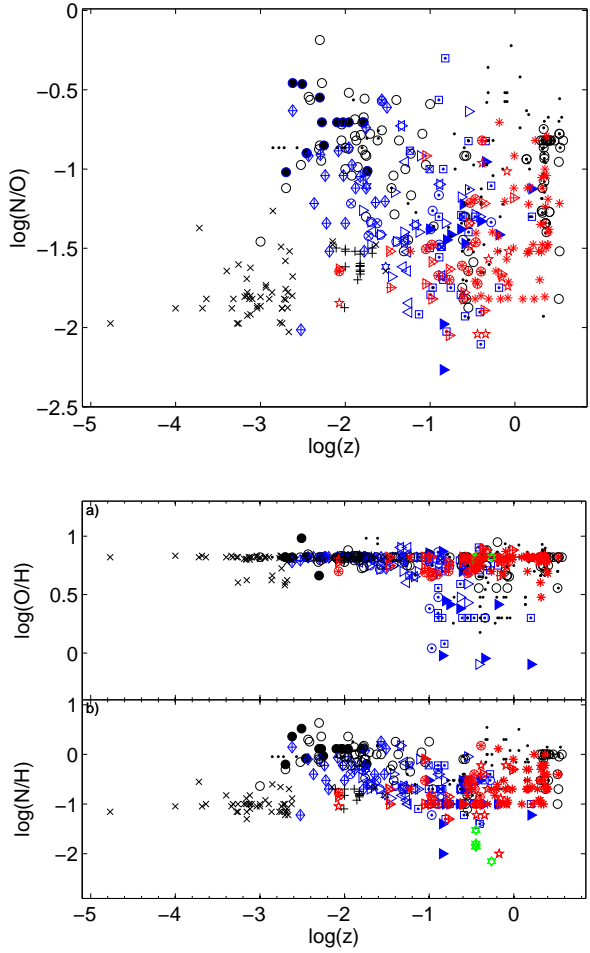


Figure 7. Top: distribution of N/O as function of the redshift for SN host galaxies (squares+filled diamonds), long GRB hosts (asterisks), short GRB hosts (stars), SB (dots), AGN (open circles) and LINERs (filled circles) both local and at higher z . Bottom : distribution of O/H and N/H as function of the redshift for SN, long GRB, short GRB, AGN, LINERs and SB hosts. Symbols as in top diagram; plus and cross : HII region galaxies nearby and local, respectively.

attains solar values at $z \sim 0.1$ (12.41 Gyr) in almost all objects, while at $z > 0.1$ the N/O ratios spread within two orders of magnitude depending on the O/H distribution. AGN and LINERs follow the SN N/O trend and extend it towards lower z , reaching N/O higher than solar.

SN hosts and AGN at $\log(O/H)+12 \leq 8.5$ are not well explained by the MC02 models. O/H in most SN hosts are nested close to solar within the N/O star-bursting formation area, but N/O in SN hosts are lower than in AGN, due to different time release of N/H and O/H.

The upper bound of the N/O trend calculated for LGRB host galaxies decreases between $z=3$ and $z=0.1$. They spread at $z > 0.3$ (10.27 Gyr) due to the N/H distribution, which ranges between solar and 0.1 solar. Massive and intermediate mass galaxies most probably coexist in this z range. At $z < 0.1$, N/O in the few LGRB hosts included in the sample follow the slowly decreasing trend calculated in nearby HII regions, while N/O calculated in SB galaxies, which coexist with LGRB hosts at $z > 0.1$, are in average higher than

solar, due to higher N/H and lower O/H. N corresponds to primary production.

Comparing LGRB hosts with SB galaxies in the N/O versus metallicity diagram (Fig. 6), N/O in SB galaxies at $\log(\text{O}/\text{H})+12$ between 8.5 and 8.82 are distributed on a large N/O range. N/O in LGRB hosts with solar O/H and $\text{N}/\text{O} < 0.1$ solar are close to those calculated in HII regions which reach $\text{N}/\text{O} \sim 0.01$. The lowest N/O are calculated in SGRB hosts, which are, however, represented by a few objects. LGRB hosts at $12+\log(\text{O}/\text{H}) < 8.5$ are included among star-bursting formation models. Some objects follow the continuous star formation trend referring to models with an infalling time $\tau_f = 4$ Gyr and a star formation timescale $\tau_{SF} = 2$ Gyr.

More data, in particular at high z , will confirm and complete our results.

ACKNOWLEDGEMENTS

I am very grateful to the referee for many critical suggestions which substantially improved the presentation of the paper.

REFERENCES

Allen, C.W. 1976 *Astrophysical Quantities*, London: Athlone (3rd edition)
 Anders, E., Grevesse, N. 1989, *Geochimica et Cosmochimica Acta*, 53, 197
 Asplund, M., Grevesse, N., Sauval, A.J., Scott, P. 2009, *ARAA*, 47, 481
 Berg, D.A. et al 2012, *ApJ*, 754, 98
 Cohen, R.D. 1983, *ApJ*, 273, 489
 Contini, M. 2017, *MNRAS*, 466, 2787
 Contini, M. 2016a, *MNRAS*, 460, 3232
 Contini, M. 2016b, *MNRAS*, 461, 2374
 Contini, M. 2015, *MNRAS*, 452, 3795
 Contini, M. 2014, *A&A*, 564, 19
 Contini, M. 1997, *A&A*, 323, 71
 Contini, T., Treyer, M.-A., Sullivan, M., Ellis, R.S. 2002, *MNRAS*, 330, 75
 de Ugarte Postigo, A. et al 2014, *A&A*, 563, 62
 Dopita, M.M. et al. 2015, *ApJS*, 217, 12
 Dors, O., Arellano-Córdova, K., Cardaci, M., Hagele, G. 2017, *MNRAS* in press
 Edmunds, M.G. & Pagel, B.E.J. 1978, *MNRAS*, 185, 777
 Edmunds, M.G. 1990, *MNRAS*, 246, 678
 Fabricant, D., Cheimets, P., Caldwell, N., Geery, J. 1998, *PASP*, 110, 79
 Gallagher, J.S., Garnavich, P.M., Berling, P., Challis, P., Jha, S., Kirshner, R.P. 2005, *ApJ*, 634, 210
 Grevesse, N., Sauval, A.J. 1998 *SSRv*, 85, 161
 Hammer, F. et al 2006, *A&A*, 454, 103
 Han, X. H., Hammer, F., Liang, Y. C., Flores, H., Rodrigues, M., Hou, J. L., Wei, J. Y. 2010, *A&A*, 514, 24
 Henry, R.B.C., Edmund, M.G. & Köppen, J. 2000, *ApJ*, 541, 660
 Kewley, L.J. & Dopita, M.M. 2002, *ApJS*, 142, 35
 Köppen, J. & Hensler, G. 2005, *A&A*, 434, 531
 Koski, A. 1978, *ApJ*, 223, 56

Kraemer, S.B., Wu, C.-C., Crenshaw, D.M., Harrington, J.P. 1994, *ApJ*, 435, 171
 Krühler, T. et al 2015 *A&A*, 581, 125
 Leloudas, G. et al 2015, *MNRAS*, 574, A61
 Marino, R.A. et al 2013, *A&A*, 559, 114
 Michalowski, M.J. et al 2016 *arXiv:1609.01742*
 Modjaz, M. et al 2008, *AJ*, 135, 1136
 Mouhcine, M., Contini, T. 2002, *A&A*, 389, 106
 Niino, Y. et al 2016 *Publ. Astron. Soc. Japan*, *arXiv:1606.01983*
 Osterbrock, D. E. 1974 in *Astrophysics of gaseous nebulae*, San Francisco, W. H. Freeman and Co., 1974.
 Pérez-Montero, E. et al. 2013, *A&A*, 549, A25
 Pérez-Montero, E. & Contini, T. 2009, *MNRAS*, 398, 949
 Pilyugin, L.S. 1993, *A&A*, 277, 42
 Piranomonte, S. et al 2015, *MNRAS*, 452, 3293
 Sanders, N.E. et al. 2012 *ApJ*, 758, 132
 Savaglio, S., Glazebrook, K., Le Borgne, D. 2009, *ApJ*, 691, 182
 Sollerman J.; Östlin, G.; Fynbo, J. P. U.; Hjorth, J.; Fruchter, A.; Pedersen, K. 2005, *NewA*, 11, 103
 Tremonti, C.A. et al. 2004, *ApJ*, 613, 898
 Vergani, S.D. et al 2011 *A&A* 535, A127
 Vila-Costas, M.B. & Edmunds, M.G. 1993, *MNRAS*, 265, 199
 Woosley, S.E. 1993, *ApJ*, 405, 273